



TECHNICAL ARTICLE

Microstructure, Texture, and Mechanical Properties of Ti6Al4V Alloy during Uniaxial Tension at Elevated Temperatures

R. Vinjamuri, B.D. Bishoyi, R.K. Sabat, M. Kumar, and S.K. Sahoo

Submitted: 12 April 2022 / Revised: 3 August 2022 / Accepted: 17 September 2022 / Published online: 3 October 2022

In the present study, the microstructure, texture and mechanical properties of Ti6Al4V (Ti64) alloy during deformation at low temperatures (i.e., around its service temperature in aerospace applications) have been investigated. The samples were subjected to uniaxial tension at temperatures of 298, 673, and 873 K for different % elongations. Refinement of both α and β grains was observed during deformation at all the studied temperatures. The α -grain refinement was identified to be of continuous dynamic recovery and recrystallization (CDRR) type. It was also found that the Burgers orientation relationship (BOR) between α and β grains refined the β grains, whereas any deviation from the relationship refined the α grains. The basal texture was observed to be tilted about 10–50° away from the normal direction (ND) of the samples after deformation. Stage III hardening was observed in the samples during deformation at all the studied temperatures. Athermal hardening was seen up to 4% deformation of the samples at a temperature of 673 K. Further, the athermal hardening rate was found to be more at 673 K deformation temperature as compared to those at 298 and 873 K due to higher activity of basal slip system at 673 K.

Keywords athermal hardening, burgers orientation relationship, EBSD, microstructure, texture, Ti-6Al-4 V, uniaxial tension

1. Introduction

Ti6Al4V, a two-phase ($\alpha + \beta$) titanium alloy, is predominantly used in aerospace applications because of its special properties, such as high temperature strength, high strength to weight ratio, excellent fatigue resistance, and fracture toughness (Ref 1-3). The alloy is mainly used as aircraft structural components and engine parts, which are subjected to different loading conditions, such as tension, shear and bending during their service operations. (Ref 4, 5). The working temperature of the alloy in aerospace applications is around 300–400 °C without losing its strength (Ref 2). The major slip systems for the HCP (Hexagonal close-packed) α -phase consist of $\{0001\}$ basal, $\{10\bar{1}0\}$ prismatic, and $\{10\bar{1}1\}$ pyramidal slip planes with $\langle 11\bar{2}0 \rangle$ as slip direction (Ref 6-9). In addition, the $\langle c + a \rangle$ type slip system comprises of $\{10\bar{1}1\}$ first order pyramidal and $\{11\bar{2}2\}$ second order pyramidal slip planes with $\langle 11\bar{2}3 \rangle$ as slip direction. The slip systems of BCC (Body-centered cubic) β -phase include $\{110\}$, $\{112\}$ and $\{113\}$ as slip planes with $\langle 111 \rangle$ as slip direction (Ref 6-9).

Although twinning is one of the important deformation modes for pure titanium and some other titanium alloys, it gets remarkably suppressed for Ti64 alloy because of its higher Al content (Ref 7, 10).

Owing to the high temperature applications of Ti64 alloy, significant research has been carried out on its microstructure and texture evolutions during deformation at elevated temperatures. The flow behavior of Ti64 alloy during hot compression tests was studied in the temperature range of 815–955 °C by Semiatin et al. (Ref 11, 12). They identified the dislocation glide/climb process as the main mechanism during deformation. Vanderhastan et al. (Ref 13) studied the deformation mechanisms of Ti64 alloy during tensile testing up to 1050 °C. For a deformation temperature from 25 to 650 °C, they found that dynamic recovery was prominent without any dynamic recrystallization. However, both dynamic recrystallization and dynamic growth were observed during deformation at higher temperatures (Ref 13). Ti64 alloy consisting of metastable α' martensite as the starting microstructure, subjected to high temperature tensile deformations within the temperature range of 700–900 °C, was studied by Matsumoto et al. (Ref 14). They found dynamic globularization was associated with an occurrence of discontinuous dynamic recrystallization. Seshacharyulu et al. (Ref 15, 16) have found the super-plasticity nature of Ti64 alloy in the temperature range of 750–950 °C during their isothermal compression tests with strain rates less than 0.0001 s^{-1} . They also identified the adiabatic shear bands in the α - β region due to flow instabilities that occurred at strain rates higher than 1 s^{-1} . The globularization response of lamellar α microstructure was studied at sub-transus and near-transus temperatures (Ref 17–19). Warwick et al. (Ref 18) conducted hot rolling experiments on β -annealed Ti64 alloy in the α - β region, i.e., at a temperature of 950 °C, and observed the softening of initial $(0002)_\alpha$ texture and kinking of α

R. Vinjamuri, B.D. Bishoyi, M. Kumar, and S.K. Sahoo, Department of Metallurgical and Materials Engineering, NIT Rourkela, Rourkela 769008, India; R.K. Sabat, School of Minerals, Metallurgical and Materials Engineering, IIT Bhubaneswar, Bhubaneswar 752050, India. Contact e-mail: sursahoo@gmail.com.

colonies. Yang and Yang (Ref 20) have studied the deformation microstructure and texture of Ti64 alloy during the hot compression process in the temperature range of 850-930 °C and strain rate range of 0.01-1 s⁻¹. They reported that dynamic recrystallization took place during deformation at high temperature (930 °C) and lower strain rates (0.01 s⁻¹). They also observed the formation of stronger texture above 930 °C, which became weaker below this temperature. Leo Prakash et al. (Ref 21) studied the effect of β -phase on microstructure and texture evolutions during hot rolling of β -quenched Ti64 alloy at 800 and 950 °C temperatures. They reported recrystallization phenomenon in β -phase and the formation of new texture

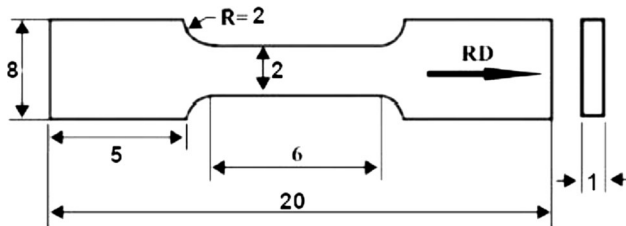


Fig. 1 Schematic of tensile specimens used in the present study (all dimensions are in mm)

component at $\phi_1 = 90^\circ$, $\Phi = 55^\circ$ and $\phi_2 = 45^\circ$ during hot rolling. Murty et al. (Ref 22) have done groove rolling experiments on Ti64 alloy and found the formation of strong $\langle 10\bar{1}0 \rangle \alpha // \text{RD}$ fiber texture at or above 650 °C. Sabat et al. (Ref 23) subjected the Ti64 plates to hot rolling at 600 and 800 °C up to 90% reduction in thickness. They found that the relative activity of pyramidal slip was higher at 600 °C than at 800 °C. They also observed the formation of a dominant basal texture irrespective of the temperature and degree of deformation. The texture components in Ti64 samples were observed to be $\{0001\} \langle 10\bar{1}0 \rangle$, $\{10\bar{1}1\} \langle 1\bar{2}10 \rangle$, $\{01\bar{1}2\} \langle 10\bar{1}0 \rangle$ and $\{01\bar{1}0\} \langle 10\bar{1}0 \rangle$ during the cold rolling experiments carried out by Jiang et al. (Ref 24). It has also been found that the presence of β -phase influences the deformation behavior of α -phase in the two-phase structure of Ti64 alloy. A Burgers orientation relationship (BOR) between the α and β phases exists, and this refines the β grains through dislocation slip transmission during deformation (Ref 25-29). However, the deviation in BOR between α and β phases refines the α grains, as suggested by Jha et al. (Ref 27).

Based on the previous studies, it is observed that most of the studies on the deformation behavior of Ti64 alloy were carried out above 600 °C and in the region of ($\alpha + \beta$) phase. It is thus important to understand the deformation behavior of the alloy

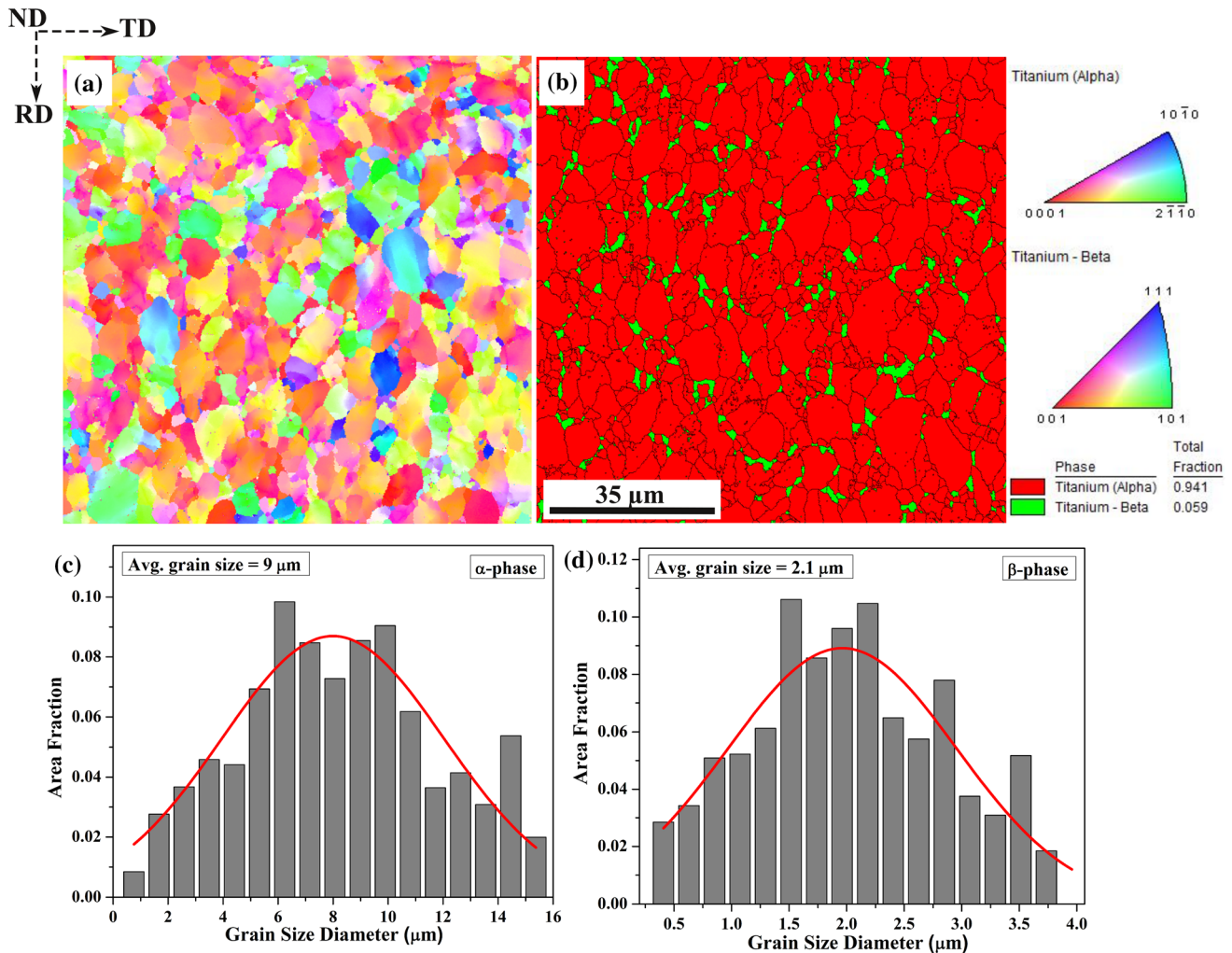


Fig. 2 Microstructure of as-received Ti64 sample before subjected to uniaxial tensile test: (a) Inverse pole figure (IPF) map; (b) Phase map; (c, d) Grain size distributions of α - and β -phases

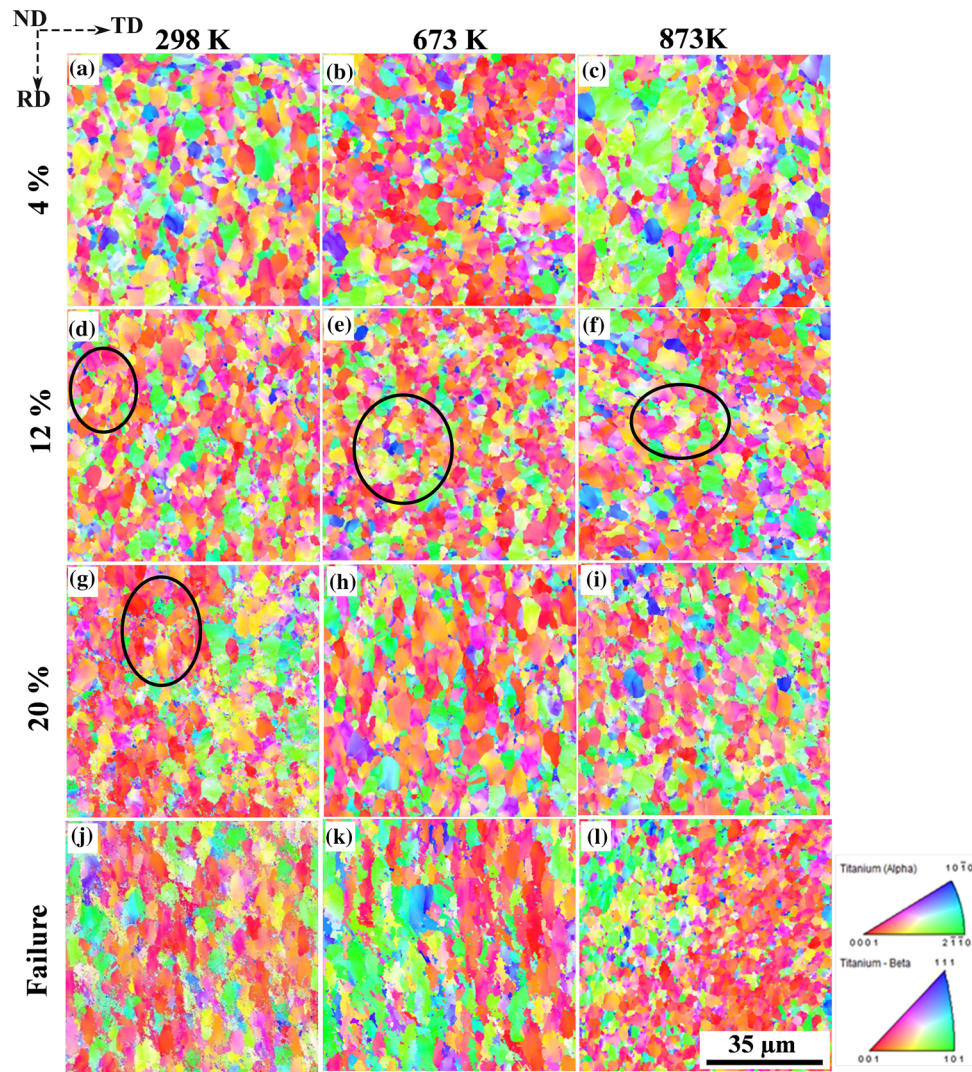


Fig. 3 IPF maps as a function of percentage elongation of the samples after uniaxial tensile tests at different temperatures. The black circled regions marked in (d, e, f, g) are further presented in Fig. 11

at lower temperatures, which are generally the service temperatures of the alloy in aerospace applications (Ref 2, 3). In the present study, the alloy has been subjected to uniaxial tension at room temperature (298 K), 400 (673 K) and 600 °C (873 K), respectively, for different % elongations to investigate its microstructure, texture and mechanical properties as a function of deformation. The effect of β -phase on the deformation behavior of the alloy has also been examined.

2. Experimental Work

2.1 Material and Sample Preparation

Ti6Al4V (grade 5) alloy sheet of 1 mm thickness was used as the starting material for the present study. Thin sheets of Ti64 are often used in making aircraft structural components and engine parts, such as low-pressure compressor blades and fan blades (Ref 2, 3). The initial sheet was cut into micro-

tensile test samples, as per the ASTM E8 standard shown in Fig. 1. The samples were subjected to uniaxial tensile tests at temperatures of 298, 673, and 873 K for deformations up to their failure. The tests were performed on an Instron 5567 screw-driven UTM (Universal Testing Machine) at a constant strain rate of $1 \times 10^{-3} \text{ s}^{-1}$. Three tensile tests were conducted at each temperature of deformation, and the average values of the test results are reported in this study. The microstructure and texture evolution after 4, 12, 20% elongations and also after the failure of the samples were examined using electron backscattered diffraction (EBSD) technique. The EBSD measurements were taken near the necking regions of samples after deformation. However, for the samples deformed up to failure, this was performed near the fracture. Samples were metallographically polished using different grits of SiC grinding papers followed by electro-polishing for EBSD characterization. Electro-polishing was carried out by using an electrolyte consisting of methanol and perchloric acid (80:20) at a temperature of $-10 \text{ }^\circ\text{C}$ and at a voltage of 25 V for 15 s time.

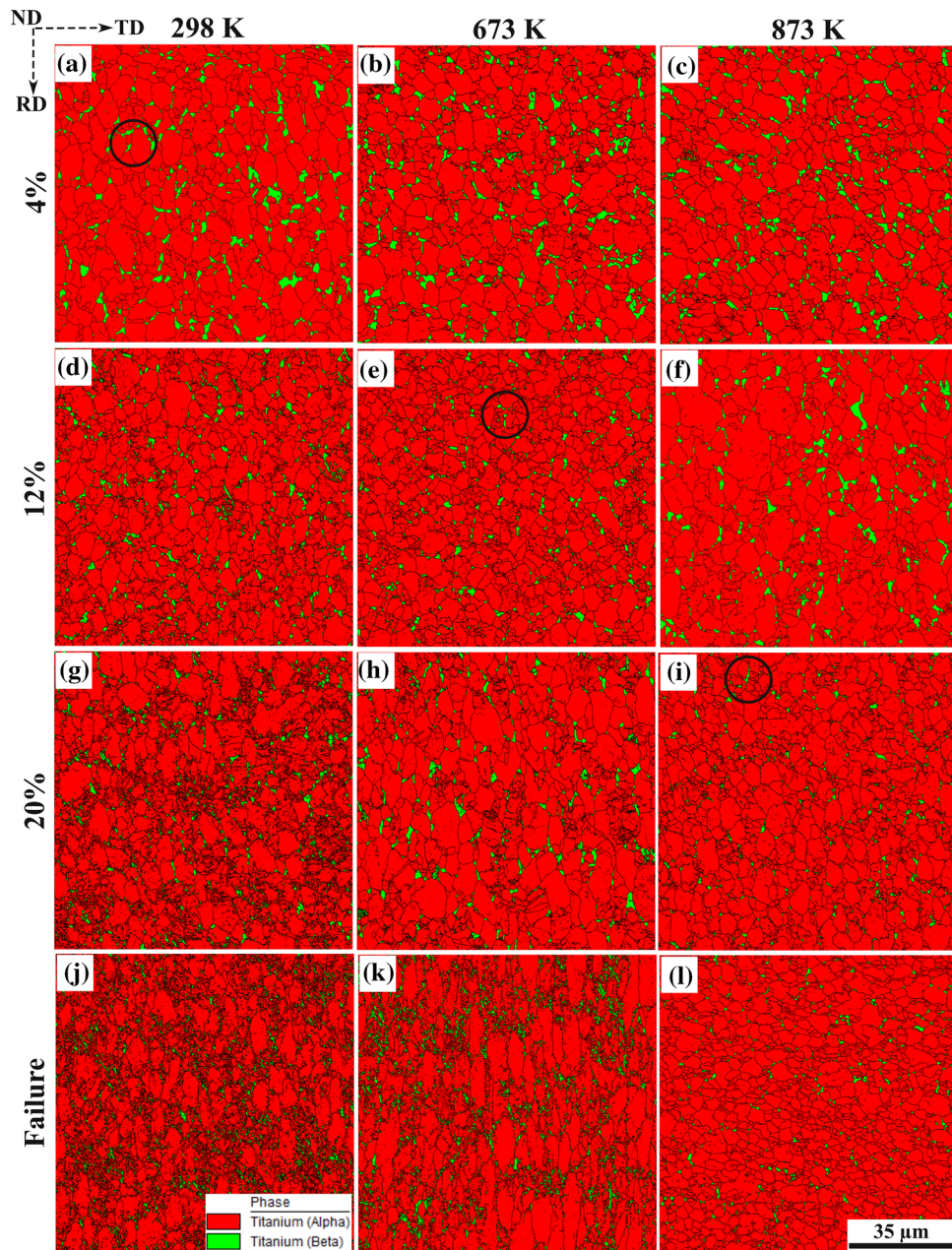


Fig. 4 Phase maps as a function of percentage elongation of the samples after uniaxial tensile tests at different temperatures. The black circled regions marked in (a, e, i) are further presented in Fig. 13

2.2 Electron Backscattered Diffraction (EBSD) Measurements

EBSD measurements were taken by using an FEI Quanta 3D FEG scanning electron microscope under the identical beam and video conditions. A step size of $0.1 \mu\text{m}$ was used for the measurements. TSL-OIM Version 6.2 software was used for the analysis of the EBSD scans. In this analysis, grains were identified based on the 15° misorientation criterion between each neighboring points. Schmidt factor for different slip/twinning systems was estimated using the TSL-OIM software. The deformation gradient for the stress state was taken as

$$\begin{pmatrix} 1 & 0 & 0 \\ 0 & 0 & 0 \\ 0 & 0 & 0 \end{pmatrix} \text{ to calculate the Schmidt factor values.}$$

3. Results

The microstructure of the as-received Ti64 sample before being subjected to uniaxial tension is shown in Fig. 2. The inverse pole figure (IPF) map and its corresponding phase map are shown in Fig. 2(a) and (b). A near-equiaxed microstructure with approximately $9 \mu\text{m}$ average grain size of α -grains was observed in the sample (Fig. 2a and c). The β -grains were found to be around 6% and were predominantly seen at the grain boundaries and the triple junctions of α -grains (Fig. 2b). The average grain size of β -grains was measured to be $\sim 2 \mu\text{m}$ (Fig. 2d). Figure 2(a) also reveals that the as-received sample had dominant near basal orientations of α -grains.

Figure 3 shows the IPF maps of the sample as a function of % elongation after uniaxial tension at different temperatures. A

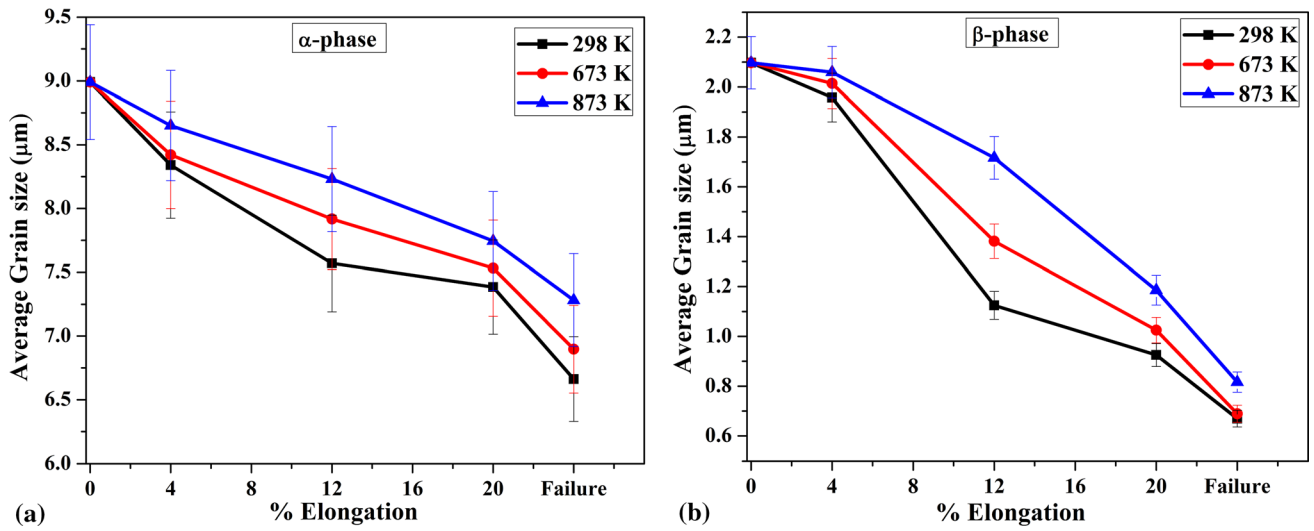


Fig. 5 Average grain sizes as a function of percentage elongation of the samples after uniaxial tension at different temperatures: (a) α -grains and (b) β -grains

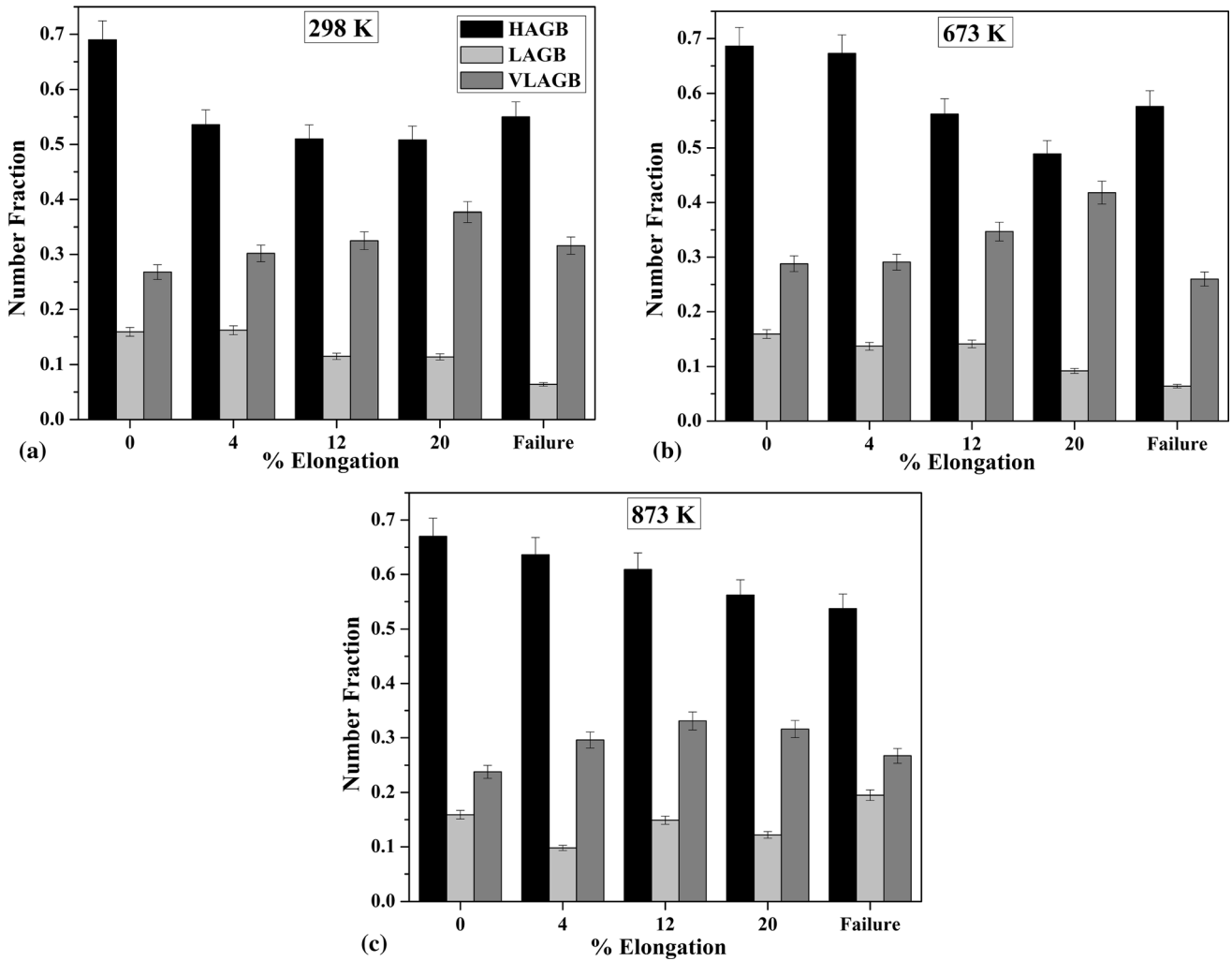


Fig. 6 Grain boundary fractions as a function of percentage elongation of the samples after uniaxial tension at temperatures of: (a) 298 K, (b) 673 K and (c) 873 K

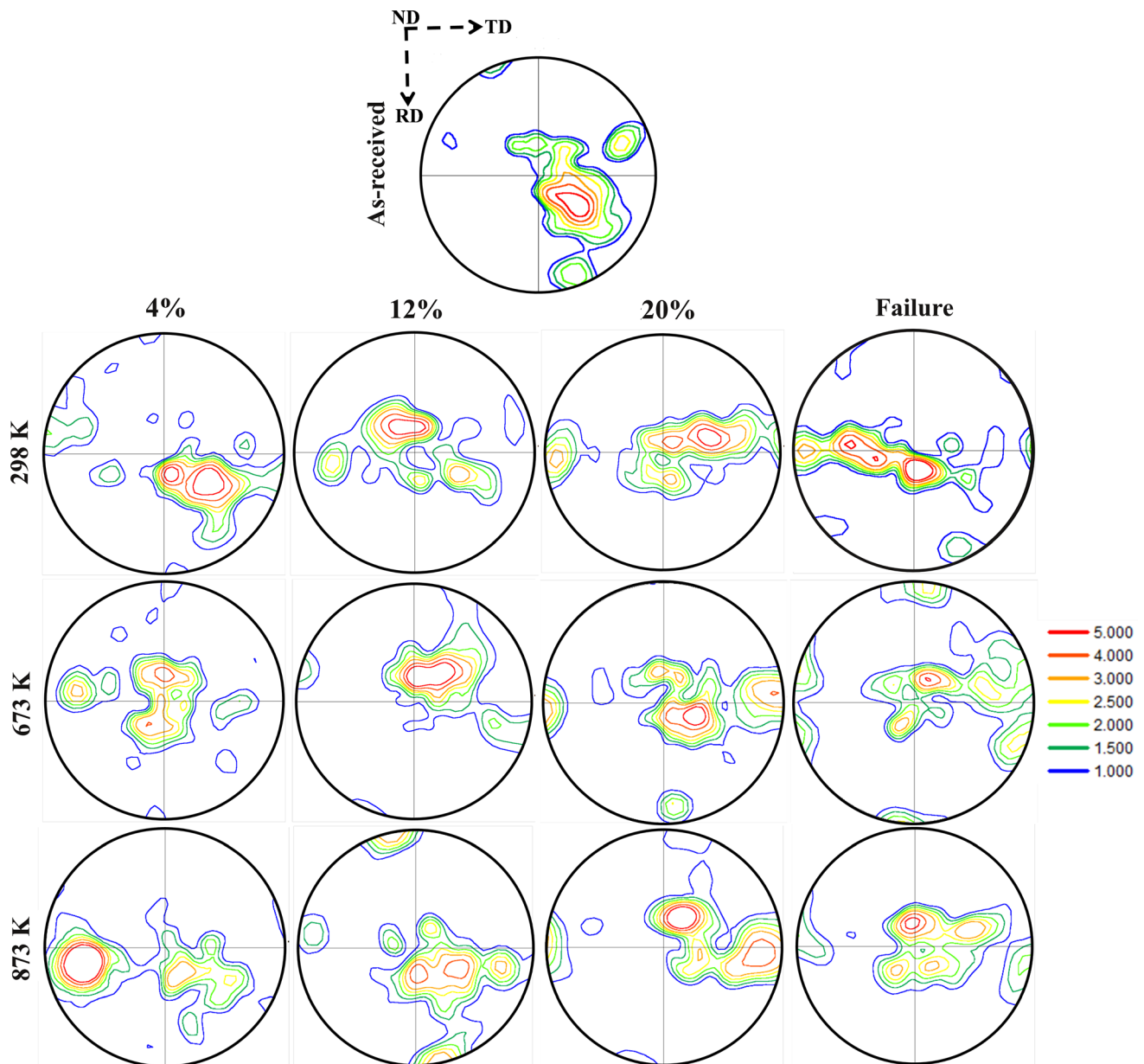


Fig. 7 (0002) pole figures of the samples as a function of percentage elongation during uniaxial tension at different temperatures

decrease in grain size without a noticeable change in the textures of the samples is observed in Fig. 3. The corresponding phase maps of the samples after deformation are presented in Fig. 4. It is seen in Fig. 4 that the β grains remained at the boundaries of α -grains and also at the triple junctions of α -grains. Also, the volume fraction of β -grains appeared to decrease with an increase in the % elongation of the samples. Figure 5 shows the average grain size of both α and β grains as a function of % elongation of the samples. A monotonous decreasing trend in grain size with an increase in % elongation of the samples was observed. The number fraction of grain boundaries, namely high angle grain boundaries (HAGB) of misorientation 15-180°, low-angle grain boundaries (LAGB) of misorientation 5-15° and very low angle grain boundaries (VLAGB) of misorientation 2-5°, are outlined in Fig. 6. A decrease in the fraction of HAGBs and an increase in the fraction of VLAGBs were observed up to 20% deformation at

all the studied temperatures. Figure 7 shows the texture developments in the form of (0002) pole figures for the samples deformed at different temperatures. The basal texture intensity was observed to be concentrated at 10-50° away from the normal direction (ND) of the samples after deformation. Figure 8 presents the orientation distribution functions (ODFs) at constant $\varphi_2 = 0^\circ$ section for the α -grains of the samples before and after deformation. Texture developments in the β grains are not included, as the volume fraction of β grains was low in the samples and their texture changes were observed to be insignificant after deformation. The as-received material had a texture concentrated at around $\varphi_1 = 165^\circ$ and $\Phi = 30^\circ$ which was along $(01\bar{1}3) < \bar{7}251 >$ orientation. After deformation at a temperature of 298 K, the initial texture component got weakened at 4% elongation. On increasing the % elongation, the texture concentration got shifted to $\varphi_1 = 90^\circ$ and $\Phi = 17^\circ$ which was along $(01\bar{1}6) < 0\bar{3}31 >$ orientation. On increasing

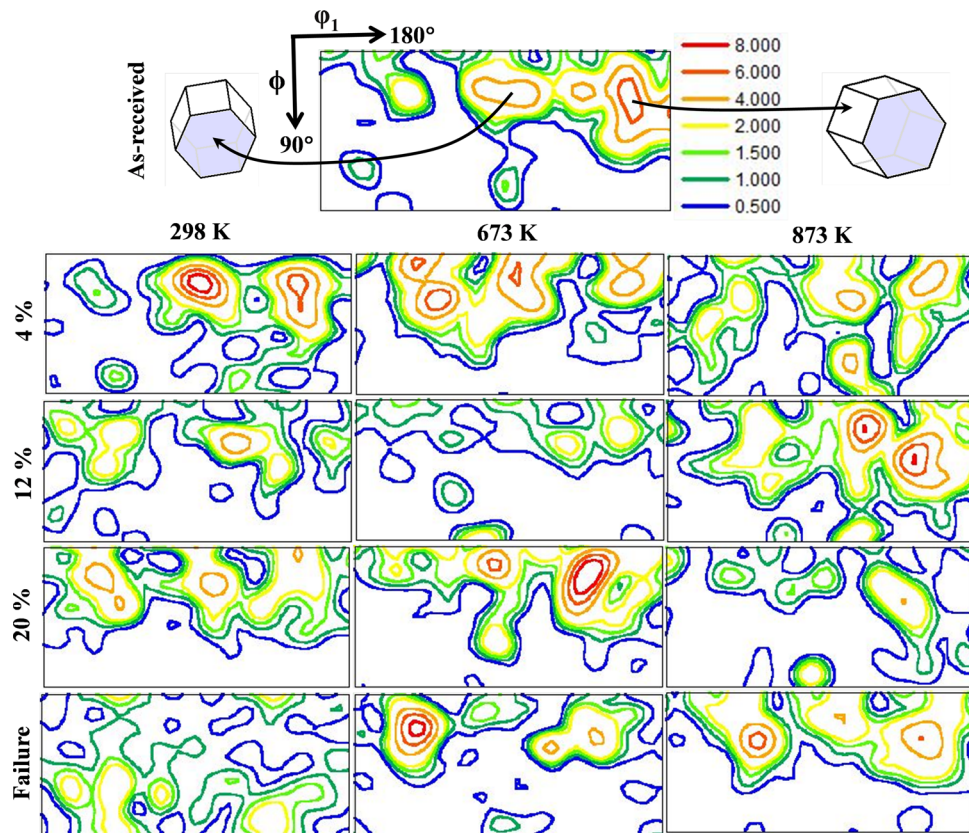


Fig. 8 ODFs, at constant $\varphi_2 = 0^\circ$, of α -grains as a function of percentage elongation of the samples after uniaxial tension at different temperatures

the % elongation at a deformation temperature of 673 K, the texture got concentrated at $\varphi_1 = 135^\circ$ and $\Phi = 20^\circ$ which was along $(01\bar{1}6)\langle 3\bar{1}41 \rangle$ orientation. At failure, the texture concentration again got shifted to $\varphi_1 = 35^\circ$ and $\Phi = 20^\circ$, i.e., along $(01\bar{1}6)\langle 5\bar{5}01 \rangle$ orientation. During deformation after 12% elongation at 873 K, the texture was observed to be concentrated at two positions, $\varphi_1 = 130^\circ$ and $\Phi = 25^\circ$, i.e., along $(01\bar{1}4)\langle 2\bar{1}31 \rangle$ orientation and also at $\varphi_1 = 40^\circ$ and $\Phi = 24^\circ$, i.e., along $(01\bar{1}4)\langle 6\bar{7}12 \rangle$ orientation. Thereafter, texture weakening was observed up to the failure of the samples.

Figure 9 represents the Schmid factor distribution of the samples during deformation at different temperatures. The Schmid factor value signifies the activity of slip systems during deformation. The active slip systems have higher Schmid factor values than the non-active slip systems. The Schmid factor for pyramidal $\langle c+a \rangle$ slip system was observed to be higher compared to the other slip systems at all the studied temperatures of deformation. It was further observed that the Schmid factors for basal and prismatic slip systems changed significantly during the plastic deformation of the samples. The true stress-strain curves and the corresponding hardening curves with respect to true stress values are shown in Fig. 10. Typical stress-strain curves (Fig. 10a) showed that the high temperature (873 K) deformed samples were plastically deformed to higher strains than those deformed at lower temperatures. Flow stress values got decreased with the rise in temperature of deformation. Figure 10(b) shows the variation of work hardening rate with true stress of the samples. Stage III hardening can be clearly seen at all temperatures of deformation. This is

attributed to the recovery process and the cross slip of dislocations during plastic deformation (Ref 30). The dislocations arrange themselves and reduce the stored energy for further deformation process. Stage III hardening is more sensitive to temperature (Ref 30, 31) and hence, the hardening rate was found to decrease with an increase in the temperature of deformation (Fig. 10).

4. Discussions

4.1 Microstructure and Texture Evolutions

To explore the possible mechanism of grain refinement at room temperature, the IPF maps after 12 and 20% deformation were examined. Figure 11 shows the magnified views of the circled regions marked in Fig. 3. However, similar observations were made from the entire microstructures of the samples during deformation. It is seen in Fig. 11 that the VLAGBs appeared adjacent to the LAGBs indicating a gradual transformation of VLAGBs to LAGBs and finally to HAGBs. Further, the fraction of HAGBs was found to decrease with an increase in the amount of strain supporting the mechanism of gradual refinement of the grains at room temperature (Ref 32, 33). A similar mechanism of grain refinement was also observed during deformation at high temperatures (673 and 873 K). However, the rate of grain refinement was seen to be reduced, which could be attributed to the annihilation of dislocations at high temperatures (Ref 34). The Schmid factor for pyramidal $\langle c+a \rangle$ slip system was almost the same at all the

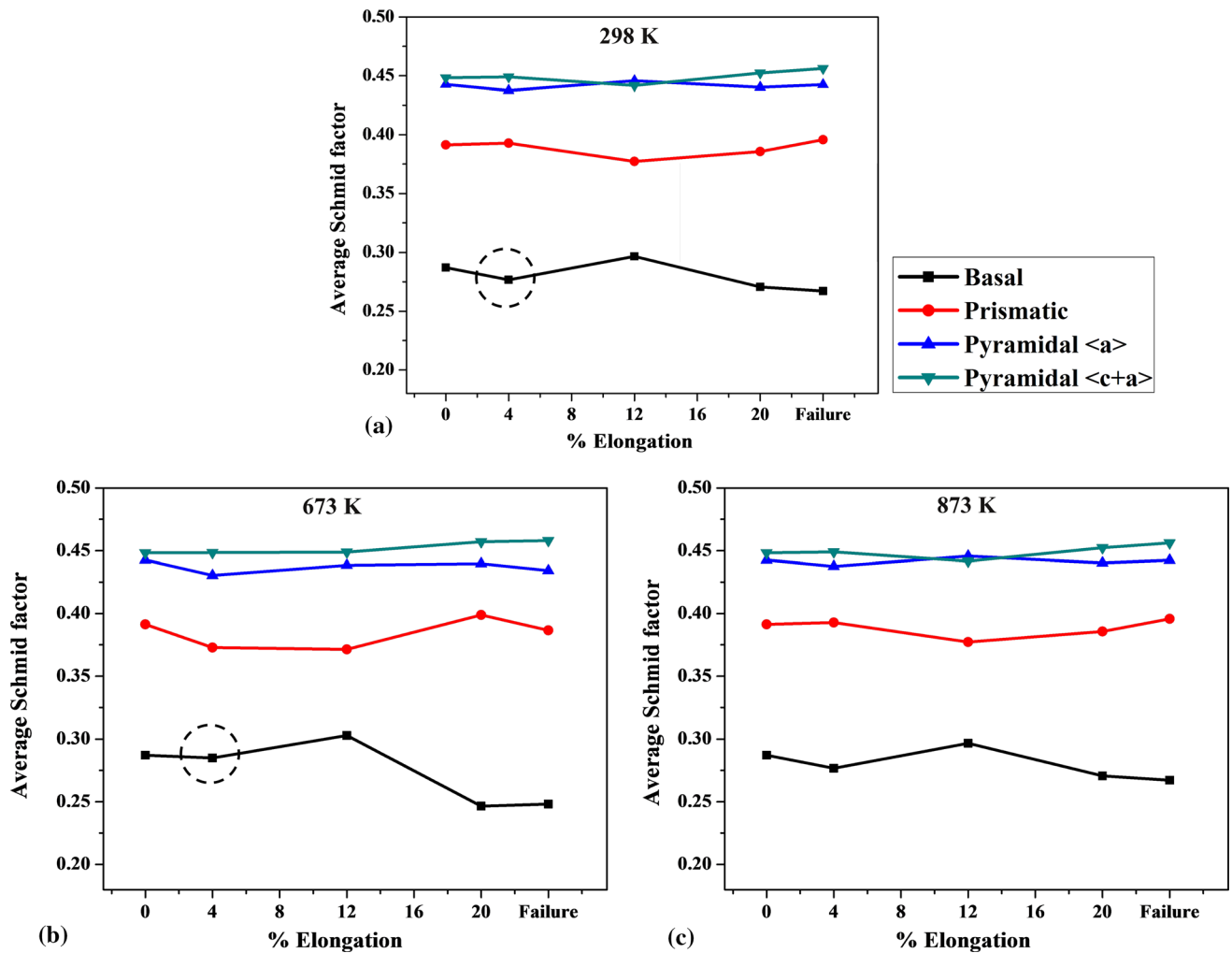


Fig. 9 Average Schmid factor values for various slip systems during uniaxial tension at temperatures of: (a) 298 K, (b) 673 K and (c) 873 K

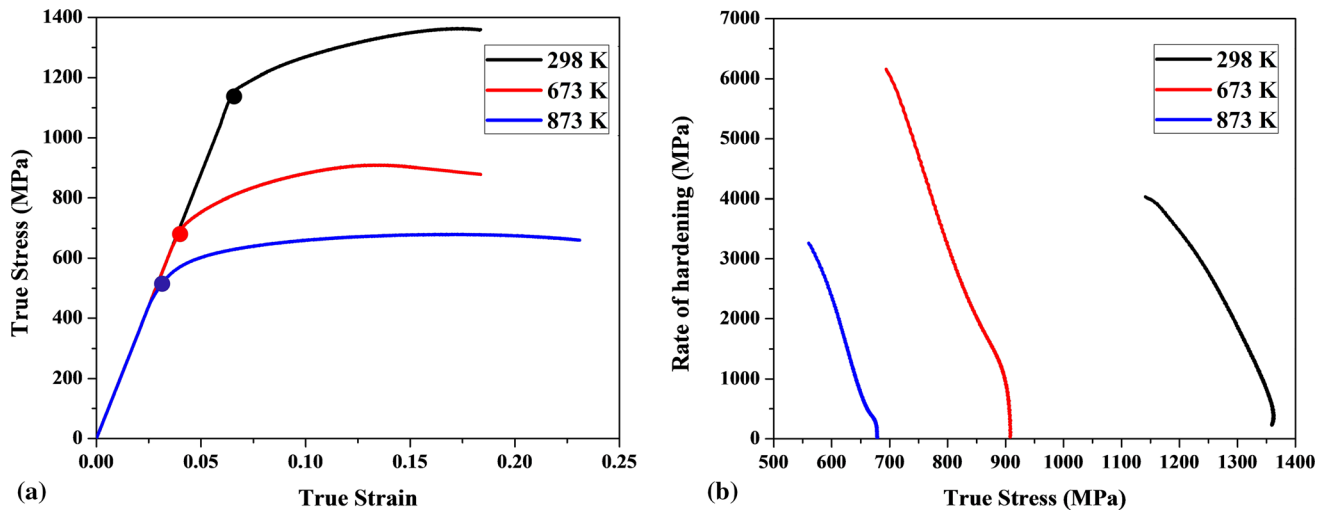


Fig. 10 (a) True stress versus true strain and (b) Work hardening rate versus true stress for the samples deformed at various temperatures

studied temperatures of deformation (Fig. 9). It indicates that the pyramidal <c+a> dislocation activity was more at high temperature as compared to room temperature because high-temperature deformation decreased the critical resolved shear

stress (CRSS) required for the activation of pyramidal <c+a> slip. It has been reported (Ref 34) that the pyramidal <c+a> dislocation being unstable decomposes into <a> and <c> type dislocations and the former par-

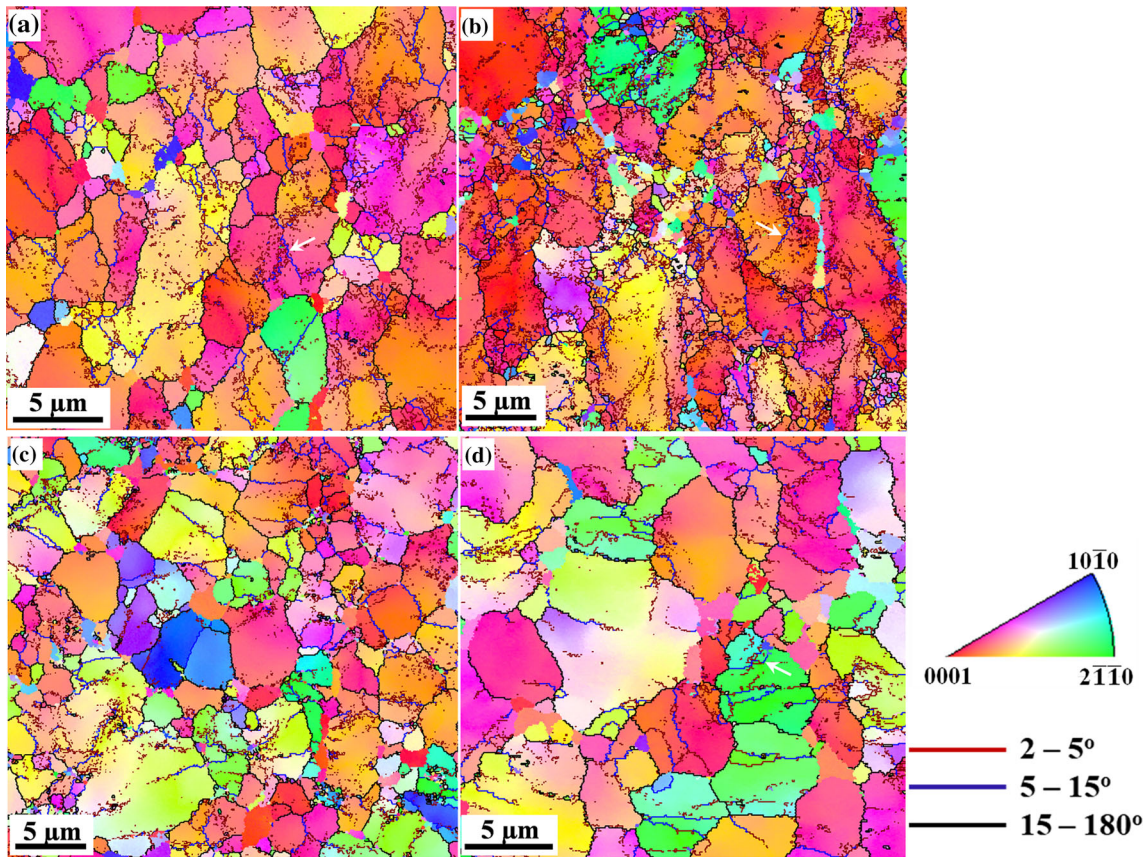


Fig. 11 Magnified views of the marked regions in Fig. 3 superimposed with grain boundaries of the samples after deformation: (a, b) 12 and 20% deformed at 298 K, (c, d) 12% deformed at 673 and 873 K. The white color arrow mark shows the presence of LAGBs adjacent to VLAGBs

icipates in the annihilation of $\langle a \rangle$ type dislocations which are already present in the material, resulting in delaying of VLAGBs to LAGBs conversion and thus delayed the grain refinement at high temperatures. The grain boundary fraction plotted in Fig. 6 supports the fact of the delayed grain refinement mechanism because the sample deformed at 673 K had a higher fraction of VLAGBs and LAGBs as compared to those deformed at room temperature. Hence, the grain refinement mechanism can be attributed to the continuous dynamic recovery and recrystallization (CDRR) type (Ref 23, 33, 35). Another mechanism of large average grain size at high temperature deformation can be attributed to the high mobility of grain boundaries, which depends on the temperature of deformation assuming the nature of the misorientation to be the same among the grains present in the microstructure (Ref 36). CDRR mechanism leads to complete recrystallization with a uniform grain structure at 873 K (Fig. 4l), whereas it induces partial recrystallization with elongated grains at 673 K temperature (Fig. 4k). To understand the dislocation activity during the CDRR mechanism, KAM (Kernel average misorientation) maps were plotted and shown in Fig. 12 for the corresponding regions shown in Fig. 11. The KAM value of each measurement point of the EBSD scan is calculated as the average misorientation of a kernel (center) point with its nearest neighbor points. It can be observed that the dislocation activity was higher near to the sub-grain boundaries (Fig. 12). Further, the dislocation activity was higher for higher % elongation of

the samples (Fig. 12b) which could be attributed to the higher number fraction of sub-grain boundaries.

It was observed that the texture intensity maxima got changed as a function of deformation strains at all the studied temperatures of deformation (Fig. 8). As no twinning was observed during the deformation of the samples (Fig. 3), the shift in texture components along φ_1 and Φ section of ODFs can be attributed to the pyramidal $\langle c + a \rangle$ and $\langle a \rangle$ type dislocation activities (Ref 23, 37). A relatively higher shift in the texture component along the Φ axis was seen up to 4% deformation at high temperatures as compared to the deformation at room temperature, indicating the higher activity of pyramidal $\langle c + a \rangle$ dislocations. The Schmid factor plot (Fig. 9) supports the above fact because the average Schmid factor values were almost the same for the samples deformed at room and high temperatures. Hence, higher activity of pyramidal $\langle c + a \rangle$ dislocation is expected at high temperature because the rise in temperature of deformation decreases the CRSS required for the activity of pyramidal $\langle c + a \rangle$ dislocation. The pyramidal $\langle c + a \rangle$ dislocation being unstable dissociates into $\langle c \rangle$ and $\langle a \rangle$ type dislocations, and the interaction of later one with other $\langle a \rangle$ types of dislocations either increases or decreases the dislocation content resulting in the grain refinement. It was observed that the sample deformed at 673 K had more athermal dislocation content (discussed in the following section) compared to the sample deformed at 298 K indicating that the extent of grain

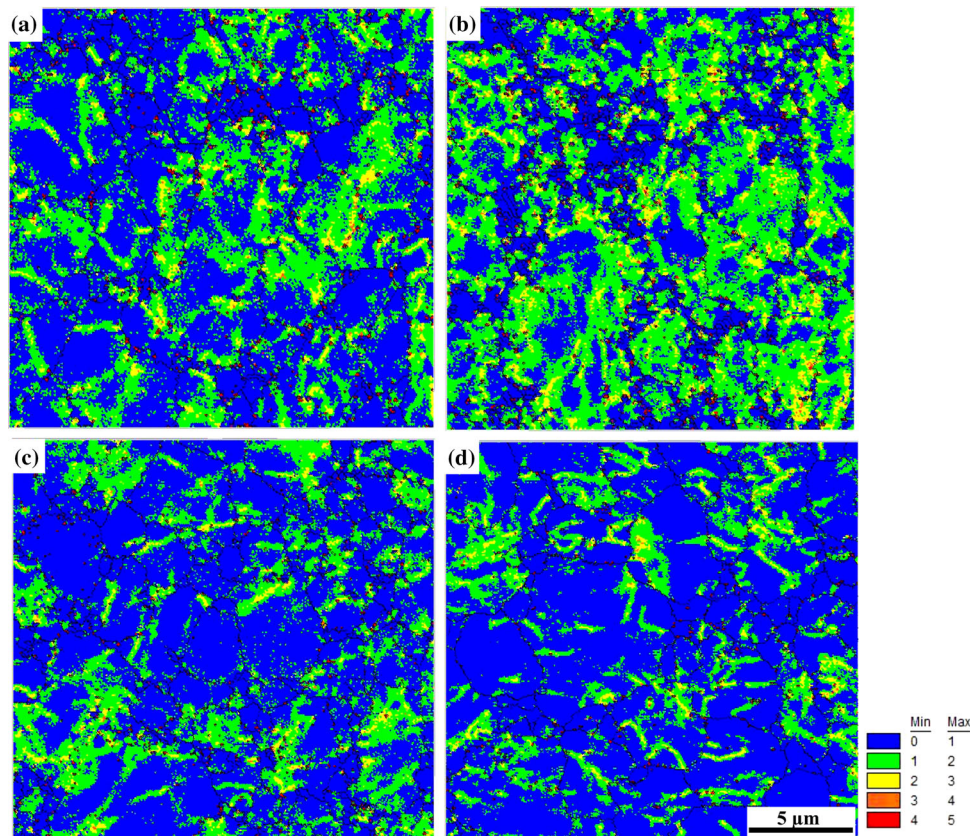


Fig. 12 KAM maps of the samples, shown in Fig. 11, after deformation: (a, b) 12 and 20% deformed at 298 K, (c, d) 12% deformed at 673 and 873 K

refinement is similar at 673 and 298 K at a strain of 4%. It is also clearly noticed from the Schmid factor values (Fig. 9) that the Schmid factor for the basal slip system was relatively higher at 673 K compared to 298 K (dotted circle in Fig. 9) after a strain of 4%.

The effect of β -phase on the grain refinement mechanism is seen in Fig. 13, which shows the magnified phase maps of samples after deformation at different temperatures. It has been suggested by Suri et al. (Ref 28) and Savage et al. (Ref 29) that the Burgers orientation relationship (BOR) between α and β phases determines the ease of dislocation slip transfer and dislocation pileup along α/β grain boundaries. A colinearity of BOR between α and β phases eases the dislocation slip transfer, while the lack of BOR develops dislocation pileup and stress concentration at α/β interface (Ref 25, 26). The crystallographic orientation relationship between α and β phases can be determined by BOR as follows: $(0001)_\alpha // (110)_\beta$ and $\langle 11\bar{2}0 \rangle_\alpha // \langle 111 \rangle_\beta$ (Ref 38, 39). In Fig. 13, the β grain along with its adjacent α grains was selected to identify the BOR between α and β phases through (0001), $(11\bar{2}0)$, (110) and (111) pole figures. It can be observed that satisfaction of BOR exists between α and β grains (Fig. 13a) and allows the dislocation slip to transfer across the α/β interface, as shown by the formation of LAGBs inside the β grains which can further transforms into HAGBs for refinement of β grains. A significant deviation in BOR was also observed between the β and α grains (Fig. 13a), and slip transfer is likely to be blocked between α and β phases resulting in dislocation pileup at the interface, as suggested by Jha et al. (Ref 27). Due to this pileup, stress concentration develops at the α/β interface

leading to dislocation rearrangement and the formation of LAGBs in α grains (Ref 27). With an increase in the extent of deformation, these LAGBs are expected to get converted into HAGBs resulting in the fragmentation of α grains.

4.2 Mechanical Property

The true stress versus strain curve indicates that the stress value decreased with a rise in the temperature of deformation (Fig. 10a). The rate of hardening was found to be higher at room temperature deformation compared to that at high temperatures (Fig. 10b). From the hardening curves, both athermal hardening (θ_0) and the value for stage III hardening (θ_{III}) were found to decrease with increase in stress value. It could also be observed that the athermal hardening rate was higher for the sample deformed at 673 K compared to the sample deformed at room temperature and 873 K (Table 1). Athermal hardening rate (marked by the circles in Fig. 10a) indicates the amount of dislocation stored in the material during deformation and was observed in the sample up to 4% deformation. The athermal hardening value was more for the sample deformed at 673 K in contrast to that at 298 K which could be attributed to the higher value of Schmid factor for the basal slip system at 673 K compared to 298 K (Fig. 9). Hence, the average grain size after 4% deformation was seen to be approximately the same for the samples deformed at 298 and 673 K. On further increase in the amount of deformation, the average grain size of the sample got decreased, but the extent of grain refinement was greater for the sample deformed at room temperature compared to that at high temperature. This could

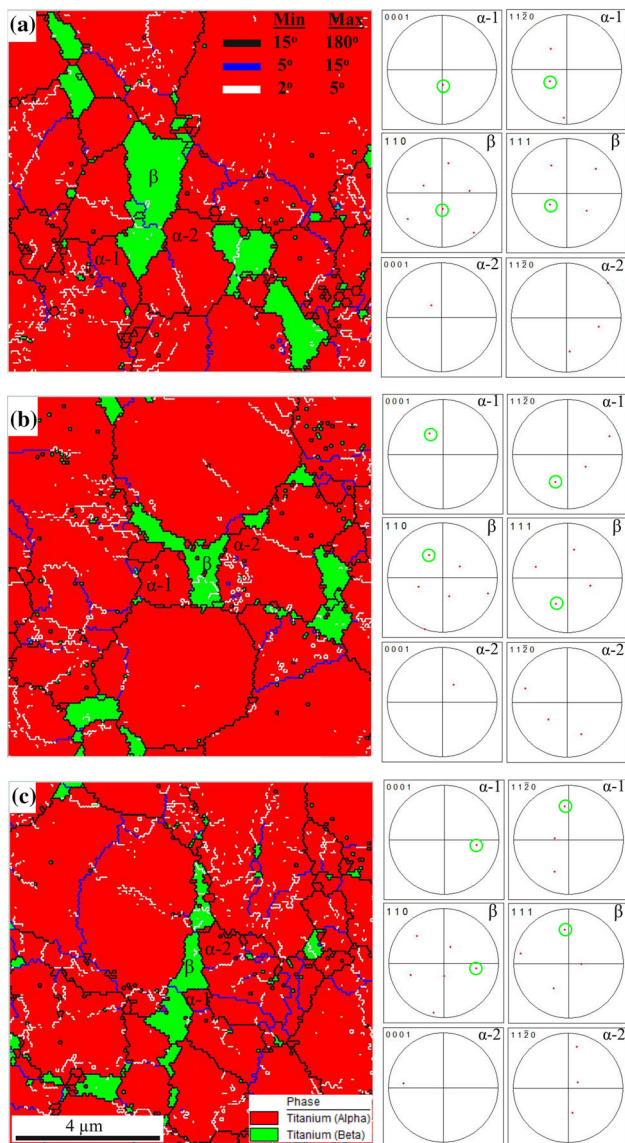


Fig. 13 Magnified views of marked regions in Fig. 4 superimposed with different grain boundaries of the samples after deformation: (a) 12% deformed at 298 K, (b) 12% deformed at 673 K and (c) 20% deformed at 873 K

Table 1 The athermal and stage III hardening rates at different temperatures of deformation

Deformation Temperature, K	θ_0	θ_{III}
273	25,290.09	- 18.00
673	27,021.08	- 29.75
873	22,506.74	- 33.50

be attributed to the rate of annihilation of dislocations, which was higher at high temperatures of deformation. The mechanical properties in terms of strength during deformation are further captured by the mean free path of the dislocations, as shown in Fig. 14. It can also be seen that just after the marked circles in Fig. 10(a), the mean free path of dislocations

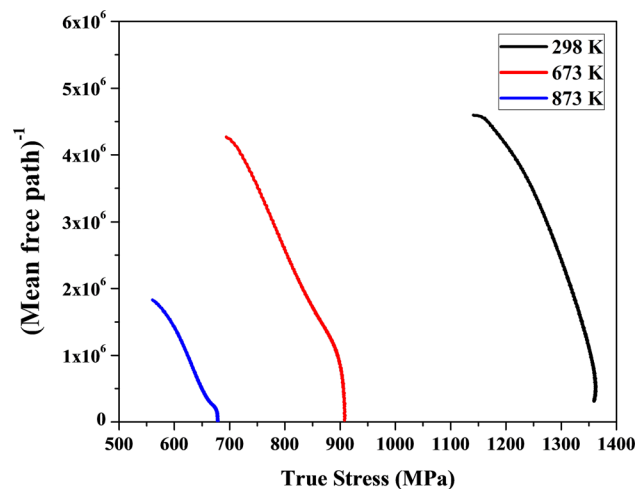


Fig. 14 Mean free path of dislocations vs true stress curves of the samples deformed at various temperatures

increases with the stress value, which indicates the annihilation of dislocations during deformation. Since no deformation twinning was observed in the samples, the annihilation of dislocation could be attributed to the increased activity of pyramidal $\langle c + a \rangle$ dislocations (Fig. 9).

5. Conclusions

Ti64 alloy has been subjected to uniaxial tension at temperatures of 298, 673 and 873 K for different % elongations, respectively. The microstructure, texture and mechanical properties of the alloy after deformation have been investigated in the present study. The observations made from the present study can be summarized as follows:

- (1) Refinement of both α and β grains was observed as a function of deformation strains at all the studied temperatures of deformation. The mechanism of such refinement in α - grains was identified to be of CDRR type. Complete recrystallization was observed during deformation at 873 K, whereas partial recrystallization was noticed at 673 K.
- (2) A BOR between α and β grains was also observed in the alloy. The satisfaction of BOR between α and β grains was found to be refined the β grains. However, any deviation from the relationship refined the α grains during deformation.
- (3) The basal texture was observed to be tilted about 10-50° away from the ND of the samples after deformation. Texture components got shifted more along Φ -axis at higher deformation temperatures compared to those at room temperature. The activity of pyramidal $\langle c + a \rangle$ slip was found to be higher during deformation at high temperatures.
- (4) Stage III hardening was observed in the samples deformed at all the temperatures. The athermal hardening was observed up to 4% deformation of the sample, and it was more at 673 K deformation temperature compared to those at 298 and 873 K. This was attributed to the higher activity of basal slip system at 673 K.

Acknowledgment

The authors thank Prof. S. Suwas, Dept. of Materials Engg., IISc Bangalore, for conducting tension tests of the samples in his Dept. The authors also thank Prof. I. Samajdar for conducting EBSD measurements of the samples in his laboratory, National Facility on OIM and Texture, Dept. of Metallurgical Engg. and Materials Science, IIT Bombay, Powai, Mumbai.

References

1. R.R. Boyer, An Overview on the Use of Titanium in the Aerospace Industry, *Mater. Sci. Eng. A.*, 1996, **213**(1–2), p 103–114
2. I. Inagaki, T. Takechi, Y. Shirai, and N. Ariyasu, Application and Features of Titanium for the Aerospace Industry, *Nippon Steel Sumitomo Metal Technical Rep.*, 2014, **106**, p 22–27
3. C. Leyens and M. Peters, *Titanium and Titanium Alloys: Fundamentals and Applications*, Wiley-VCH, Weinheim, 2003
4. E. Do Nascimento Filho, V.A.R. Henriques, J.L. de Oliveira, and E.F. Diniz, Microstructural Study of Ti-6Al-4V Produced with TiH₂ Powder, SAE Tech. Pap. Ser., (2012), 36, p. 0197
5. T.H.G. Megson, *Aircraft Structures for Engineering Students*, Edward Arnold, London, 1972
6. D.G.L. Prakash, R. Ding, R.J. Moat, I. Jones, P.J. Withers, J. Quinta, and M. Preuss, Deformation Twinning in Ti-6Al-4V During Low Strain Rate Deformation to Moderate Strains at Room Temperature, *Mater. Sci. Eng. A.*, 2010, **527**(21–22), p 5734–5744
7. G. Luetjering, *Titanium*, 2nd eds. (Springer, New York, 2007)
8. D. Banerjee and J. Williams, Microstructure and slip character in titanium alloys, *Def. Sci. J.*, 1986, **36**(2), p 191–206
9. A. Lewis, S. Qidwai, and A. Geltmacher, Slip Systems and Initiation of Plasticity in a Body Centred Cubic Titanium Alloy, *Metall. Mater. Trans. A.*, 2010, **41**(10), p 2522–2531
10. J. Galan-Lopez, S. Naghdy, P. Verleysen, L. Kestens, F. Coghe, L. Rabet, and J. Degrieck, Mechanical Behavior And Texture Prediction of Ti-6Al-4V Based on Elastic Viscoplastic Self-Consistent Modelling, in *IOP Conference Series: Materials Science and Engineering*, vol 82, August 24–29, 2014 (Dresden, Germany, 2015) p. 012027
11. S.L. Semiatin, V. Seetharaman, and I. Weiss, Flow Behavior and Globularization Kinetics During Hot Working of Ti-6Al-4V with a Colony Alpha Microstructure, *Mater. Sci. Eng. A.*, 1999, **263**(2), p 257–271
12. S.L. Semiatin and T.R. Bieler, The Effect of Alpha Platelet Thickness on Plastic Flow During hot Working of Ti-6Al-4V with a Transformed Microstructure, *Acta Mater.*, 2001, **49**(17), p 3565–3573
13. M. Vanderhastan, L. Rabet, and B. Verlinden, Deformation Mechanisms of Ti-6Al-4V During Tensile Behavior at Low Strain Rate, *J. Mater. Eng. Perform.*, 2007, **16**, p 208–212
14. H. Matsumoto, T. Nishihara, Y. Iwagaki, T. Shiraiishi, and Y. Ono, Microstructural Evolution and Deformation Mode Under High-Temperature-Tensile-Deformation of the Ti-6Al-4V Alloy with the Metastable α' Martensite Starting Microstructure, *Mater. Sci. Eng. A.*, 2016, **661**, p 68–78
15. T. Seshacharyulu, S.C. Medeiros, W.G. Frazier, and Y.V.R.K. Prasad, Hot Working of Commercial Ti-6Al-4V with an Equiaxed α - β Microstructure: Material Modeling Considerations, *Mater. Sci. Eng. A.*, 2000, **284**(1–2), p 184–194
16. T. Seshacharyulu, S.C. Medeiros, W.G. Frazier, and Y.V.R.K. Prasad, Microstructural Mechanisms During Hot Working of Commercial Grade Ti-6Al-4V with Lamellar Starting Structure, *Mater. Sci. Eng. A.*, 2002, **325**(1–2), p 112–125
17. Z.X. Zhang, S.J. Qu, A.H. Feng, J. Shen, and D.L. Chen, Hot Deformation Behavior of Ti-6Al-4V Alloy: Effect of initial Microstructure, *J. Alloys Compd.*, 2017, **718**, p 170–181
18. J.L.W. Warwick, N.G. Jones, I. Bantounas, M. Preuss, and D. Dye, In Situ Observation of Texture and Microstructure Evolution during Rolling and Globularization of Ti-6Al-4V, *Acta Mater.*, 2013, **61**(5), p 1603–1615
19. B. Perumal, M.A. Rist, S. Gungor, J.W. Brooks, and M.E. Fitzpatrick, The Effect of Hot Deformation Parameters on Microstructure Evolution of the α -Phase in Ti-6Al-4V, *Metall. Mater. Trans. A.*, 2016, **47**, p 4128–4136
20. L. Yang and Y. Yang, Deformed Microstructure, and Texture of Ti6Al4V Alloy, *Trans. Nonferrous Met. Soc. China.*, 2014, **24**(10), p 3103–3110
21. D.G.L. Prakash, P. Honniball, D. Rugg, P.J. Withers, J. Quinta, and M. Preuss, The Effect of β Phase on Microstructure and Texture Evolution during Thermomechanical Processing of $\alpha + \beta$ Ti Alloy, *Acta Mater.*, 2013, **61**(9), p 3200–3213
22. S.V.S.N. Murty, N. Nayan, P. Kumar, P.R. Narayanan, S.C. Sharma, and K.M. George, Microstructure-Texture-Mechanical Properties Relationship in Multi-Pass Warm Rolled Ti-6Al-4V Alloy, *Mater. Sci. Eng. A.*, 2014, **589**, p 174–181
23. R.K. Sabat, M.V.S.S.D.S.S. Pavan, D.S. Aakash, M. Kumar, and S.K. Sahoo, Mechanism of Texture and Microstructure Evolution During Warm Rolling of Ti-6Al-4V Alloy, *Philos. Mag.*, 2018, **98**(28), p 2562–2581
24. H. Jiang, P. Dong, S. Zeng, and B. Wu, Effects of Recrystallization on Microstructure and Texture Evolution of Cold-Rolled Ti-6Al-4V Alloy, *J. Mater. Eng. Perform.*, 2016, **25**(5), p 1931–1938
25. S. Roy and S. Suwas, Microstructure and Texture Evolution During Sub-Transus Thermomechanical Processing of Ti-6Al-4V-0.1B Alloy: Part I. Hot Rolling in ($\alpha + \beta$) Phase Field, *Metall. Mater. Trans. A.*, 2013, **44**(7), p 3303–3321
26. X. Ji, B. Guo, F. Jiang, H. Yu, D. Fu, J. Teng, H. Zhang, and J.J. Jonas, Accelerated Flow Softening and Dynamic Transformation of Ti-6Al-4V Alloy in Two-Phase Region During Hot Deformation Via Coarsening α Grain, *J. Mater. Sci. Technol.*, 2020, **36**, p 160–166
27. J.S. Jha, S. Dhala, S.P. Toppo, R. Singh, and A. Tewari, Effect of Strain Amplitude on Low Cycle Fatigue and Microstructure Evolution in Ti-6Al-4V: A TKD and TEM Characterization, *Mater. Charact.*, 2019, **155**, p 109829
28. S. Suri, G.B. Viswanathan, T. Neeraj, D.H. Hou, and M.J. Mills, Room Temperature Deformation and Mechanisms of Slip Transmission in Oriented Single-Colony Crystals of α/β Titanium Alloy, *Acta Mater.*, 1999, **47**(3), p 1019–1034
29. M.F. Savage, J. Tatalovich, and M.J. Mills, Anisotropy in the Room-Temperature Deformation of α - β Colonies in Titanium Alloys: Role of the α - β Interface, *Philos. Mag.*, 2004, **84**(11), p 1127–1154
30. A.D. Rollett, U.F. Kocks, and R.D. Doherty, Formability and Metallurgical Structure, in: eds. by A.K. Sachdev, J.D. Embury, The Metall. Society, (1987), p. 211
31. H. Jiang, P. Dong, S. Zeng, and B. Wu, Effects of Recrystallization on Microstructure and Texture Evolution of Cold-Rolled Ti-6Al-4V Alloy, *J. Mater. Eng. Perform.*, 2016, **25**, p 1931–1938
32. R.K. Sabat, P.K. Samal, and S. Muzzamil Ahamed, Effect of Strain Path on the Evolution of Microstructure Texture and Tensile Properties of WE43 Alloy, *Mater. Sci. Eng. A*, 2018, **715**, p 348–358
33. S. Biswas, D.-I. Kim, and S. Suwas, Asymmetric and Symmetric Rolling of Magnesium: Evolution of Microstructure, Texture and Mechanical Properties, *Mater. Sci. Eng. A*, 2012, **550**, p 19–30
34. J. Geng, M.F. Chisholm, R.K. Mishra, and K.S. Kumar, An Electron Microscopy Study of Dislocation Structures in Mg Single Crystals Compressed Along [0 0 0 1] at Room Temperature, *Philos. Mag.*, 2015, **95**(35), p 3910–3932
35. L. Jin, D. Lin, D. Mao, X. Zeng, B. Chen, and W. Ding, Microstructure Evolution of AZ31 Mg Alloy During Equal Channel Angular Extrusion, *Mater. Sci. Eng. A*, 2006, **423**(1–2), p 247–252
36. D. Panda, R.K. Sabat, S. Suwas, V.D. Hiwarkar, and S.K. Sahoo, Texture Weakening in Pure Magnesium During Grain Growth, *Philos. Mag.*, 2019, **99**(11), p 1362–1385
37. B.D. Bishoyi, R.K. Sabat, and S.K. Sahoo, Effect of Temperature on Microstructure and Texture Evolutions During Uniaxial Compression of Commercially Pure Titanium, *Mater. Sci. Eng. A.*, 2018, **718**, p 398–411
38. N. Stanford and P.S. Bate, Crystallographic Variant Selection in Ti-6Al-4V, *Acta Mater.*, 2004, **52**(17), p 5215–5224
39. D. Bhattacharyya, G.B. Viswanathan, R. Denkenberger, D. Furrer, and H.L. Fraser, The Role of Crystallographic and Geometrical Relationships Between α and β Phases in an α/β Titanium Alloy, *Acta Mater.*, 2003, **51**(16), p 4679–4691

Publisher's Note Springer Nature remains neutral with regard to jurisdictional claims in published maps and institutional affiliations.